RSC Advances

PAPER

View Article Online
View Journal | View Issue

Cite this: *RSC Adv.*, 2017, **7**, 37689

Catalytic effect of MoS_2 on hydrogen storage thermodynamics and kinetics of an as-milled $YMg_{11}Ni$ alloy

Yanghuan Zhang,[*ab] Meng Ji,[ab] Zeming Yuan,[ab] Wengang Bu,[b] Yan Qi[b] and Shihai Guo[b]

In this study, $YMg_{11}Ni$ and $YMg_{11}Ni$ + 5 wt% MoS_2 (named $YMg_{11}Ni-5MoS_2$) alloys were prepared by mechanical milling to examine the effect of adding MoS_2 on the hydrogen storage performance of a Y–Mg–Ni-based alloy. The as-cast and milled alloys were tested to identify their structures by X-ray diffraction and transmission electron microscopy. The isothermal hydrogen storage thermodynamics and dynamics were identified through an automatic Sieverts apparatus, and the non-isothermal dehydrogenation performance was investigated by thermogravimetry and differential scanning calorimetry. The dehydrogenation activation energy was calculated by both Arrhenius and Kissinger methods. Results revealed that adding MoS_2 produces a very slight effect on hydrogen storage thermodynamics but causes an obvious reduction in the hydrogen sorption and desorption capacities because of the deadweight of MoS_2. The addition of MoS_2 significantly enhances the dehydrogenation performance of the alloy, such as lowering dehydrogenation temperature and enhancing dehydrogenation rate. Specifically, the initial desorption temperature of the alloy hydride lowers from 549.8 K to 525.8 K. The time required to desorb hydrogen at 3 wt% H_2 is 1106, 456, 363, and 180 s corresponding to hydrogen desorption temperatures at 593, 613, 633, and 653 K for the $YMg_{11}Ni$ alloy, and 507, 208, 125, and 86 s at identical conditions for the $YMg_{11}Ni-5MoS_2$ alloy. The dehydrogenation activation energy (E_a) values with and without added MoS_2 are 85.32 and 98.01 kJ mol^{-1}. Thus, a decrease in E_a value by 12.69 kJ mol^{-1} occurs and is responsible for the amelioration of the hydrogen desorption dynamics by adding a MoS_2 catalyst.

Received 28th May 2017
Accepted 25th July 2017

DOI: 10.1039/c7ra05965e

rsc.li/rsc-advances

Introduction

The wide application of hydrogen as a clean fuel is believed to largely offset environmental problems that result from the mass consumption of fossil fuels. The rapid development and extensive application of hydrogen fuel cell vehicles are expected to fundamentally alleviate accelerating global warming and the increasingly serious air pollution because the combustion of fossil fuels is related to the consumption of approximately a quarter of the energy of the whole world[1] and the emission of approximately 23% of global CO_2.[2] However, the application of hydrogen as vehicle fuel is seriously limited, because hydrogen storage systems are not safe and are inefficient.[3] In other words, whether the hydrogen fuel cell vehicle will be widely applied in this century depends on its safety, economics, and practical hydrogen storage capacity.[4] Storing hydrogen in metal hydrides is the preferred candidate among the known hydrogen storage methods and is expected to make mobile application possible.[5] Many hydrogen storage materials have been established, and some of them even have been commercialized on a large scale. These materials are rare earth-based AB_5 and Laves-phase AB_2 alloys. However, selecting which material could satisfy the performance requirements for vehicular application presented by the U.S. Department of Energy is difficult.[6] Concerning hydrogen storage capacity, Mg and Mg-based alloys show their preponderances for on-board hydrogen fuel cell.[7] However, the practical application of Mg and Mg-based alloys is restricted severely by some inherent disadvantages, including the high thermodynamic stability and slow hydrogen absorption/desorption dynamics. Therefore, the researchers must exert considerable effort to further improve these hydrogen storage properties of the Mg-based alloys.

Based on the summary of numerous literatures, the two major approaches to improve the Mg and Mg-based alloys in hydrogen storage performances are reducing the particle size and adding catalysts (elements or compounds) to form Mg-based composites or solid solution. Ouyang *et al.*[8–10] found the P-milling technique can tune thermodynamic and kinetic

[a]*Key Laboratory of Integrated Exploitation of Baiyun Obo Multi-Metal Resources, Inner Mongolia University of Science and Technology, Baotou 014010, China. E-mail: zhangyh59@sina.com*

[b]*Department of Functional Material Research, Central Iron and Steel Research Institute, Beijing 100081, China*

properties of Mg-based hydrogen storage materials. The structures of Mg and Mg-based alloys have obvious effects on their hydrogen absorption/desorption thermodynamics and dynamics.[11] The formation of composite microstructures can substantially improve the hydrogen storage properties of Mg-based alloys.[12] In particular, when the grain sizes of Mg-based alloys are far below micrometer scale, their hydriding/dehydriding performances will be improved dramatically.[13,14] Kumar *et al.*[15] found that ultrafine microstructure (sub 100 nm range) decreases Mg_2Ni alloy by 100 K in the hydrogen absorption/desorption temperature, that is, from 573 K to 473 K. This result was also affirmed by Cheung *et al.*[16] that the stability of MgH_2 drops quickly when its particle size reduces to nanoscale. The hydrogen atom diffusion distance for traversing the hydride is shortened relatively as a result of the small scales and high surface area-to-volume ratio belonging to the nanostructured powders, thereby improving the hydrogenation dynamics by several times and even more.[17] Some synthetic methods, such as arc plasma,[18] equal channel angular pressing (ECAP),[19] inert gas condensation (IGC),[20] hydriding combustion synthesis,[21] mechanical milling,[22,23] and rapid solidification (RS),[24,25] have been widely used in the syntheses of different amorphous and nanocrystalline Mg-based alloys with various ingredients. Among all of the techniques, mechanical milling and melt spinning are considered to be fairly effective by which the amorphous and/or nanocrystalline alloys can be obtained with homogeneous element distributions. Poletaev *et al.*[26] prepared the $LaMg_{11}Ni$ alloy using rapid solidification technology and found that $LaMg_{11}Ni$ alloy that solidified at the highest cooling rate exhibited the best hydriding dynamics and reached the maximal hydrogen absorption capacity of 5.02 wt% H_2. Jeon *et al.*[27] prepared a composite, of which the Mg nanoparticle was more than 60 wt% and dispersed in a dissolved polymer. They also found that the hydrogen absorption and desorption could occur in this composite with a fast dynamics below 473 K.

In general, rare earth elements,[18] transition metallic elements[28] and their oxides,[29–31] fluorides,[32,33] halides,[34] hydrides,[35] and intermetallic compounds,[36] are good catalysts that can destabilize MgH_2 and enhance the hydriding and dehydriding rate of the alloy hydrides. The dissociation of hydrogen molecules on the Mg surface is considered a rate-controlling factor for dehydrogenation because of the high energy (1.15 eV) required. This dissociation energy can be reduced by adding catalysts. For example, the presence of transition metals, such as Pd, Cu, Ni, and Co, can reduce dissociation energy to 0.39, 0.56, 0.06, and 0.03 eV, respectively.[37] Theoretically, the substitutional atoms in MgH_2 can cause an interaction between the valence electron of H and the unsaturated d/f electron shells of transition metals, which will weaken the Mg–H bond. Thus, the hydrogen desorption behavior of MgH_2 is ameliorated significantly.[38] In addition, some catalysts with high hardness also play the role of cracking agent during ball milling so that the size of alloy particles can be reduced dramatically.[39] The advantageous effect of reducing particle size on hydrogen sorption and desorption properties has been described. Sadhasivam *et al.*[13] investigated the effect of adding Mm (the major ingredients are Ce and La) oxide on the dehydrogenation dynamics of MgH_2 and found that it improved hydrogenation behavior. The initial dehydrogenation temperature for MgH_2 catalyzed by 5 wt% Mm oxide obtained a decrease of 349 K, that is, from 654 K (ball-milled) to 578 K. Daryani *et al.*[40] reported that adding TiO_2 catalysts can significantly enhance the milling efficiency and accelerate the size reduction of MgH_2 during ball milling. Moreover, the addition of 6 mol% TiO_2 markedly improved the hydrogen absorption dynamics and decreased the decomposition temperature of as-milled MgH_2 by 373 K.

Our previous work has investigated the thermodynamics and dynamics of the $REMg_{11}Ni$ (RE = La, Nd, Pr) + x wt% Ni (x = 100, 200) alloys and found that Ni addition exhibits an effective catalytic action on ameliorating the hydrogen storage properties of $REMg_{11}Ni$ (RE = La, Nd, Pr) alloys.[41–43] However, the hydrogenation thermodynamics and dynamics ameliorated by adding Ni negatively affected capacity. Han *et al.*[44,45] found MoS_2 has superior properties on catalyzing the hydriding/dehydriding kinetics of MgH_2 and markedly decreases the decomposition temperature of $LiBH_4$. To avoid the lowering of hydrogen adsorption capacity because of excessive Ni, a trace of MoS_2 is added in $YMg_{11}Ni$ as catalyst. In the present work, $YMg_{11}Ni$ alloy is investigated for its phase composition, microstructure, catalytic hydrogen desorption temperature, and activation energy to study the effects of MoS_2 on hydrogen storage thermodynamics and kinetics of as-milled $YMg_{11}Ni$ alloy.

Experimental

$YMg_{11}Ni$ alloy was prepared in a vacuum induction furnace with 0.04 MPa protective gas of helium for preventing the volatilization of Mg. The liquid alloy was cast into ingots with a cooled copper mould. Portions of the ingots were severed and crushed into powders with diameters of approximately 50 μm. After crushing, 5 wt% MoS_2 (particle size ≤ 30 nm, Sinopharm Chemical Reagent Co., Ltd) was added and a planetary-type mill was used for milling this mixed powder. During ball milling, the argon atmosphere was selected to fill up the mill to prevent the oxidation of mixed powders. In this experiment, the ball-to-powder weight ratio was 35 : 1, in which the balls and powders were placed into Cr–Ni stainless steel vials and ran at 135 rpm for 20 h. During the whole process, the mill had a 10 min rest after every 60 min milling to prevent overheating.

The X-ray diffraction (XRD) (D/max/2400) equipped with $CuK_{\alpha 1}$ radiation filtered by graphite was used to test the as-cast and milled alloys of their phase structures. The experimental parameters of XRD were set at 160 mA, 40 kV, and 10° min^{-1}. High-resolution transmission electron microscope (HRTEM) (JEM-2100F) was used to observe the powder samples at 200 kV. Electron diffraction (ED) was used to ascertain their crystalline states.

An automatically controlled Sieverts apparatus was used to measure the isothermal hydriding and dehydriding dynamics with the temperature error controlled within ±2 K. The weight of samples for each measurement was 300 mg. The hydrogenation reaction proceeded in 3 MPa hydrogen (initial pressure

for hydrogenation reaction) at 593, 613, 633, and 653 K, at similar temperatures at which the dehydrogenation process proceeded with the hydrogen pressure setting at 1×10^{-4} MPa. Thermogravimetry and differential scanning calorimetry (DSC) (SDT-Q600) were used to investigate the non-isothermal dehydrogenation performance with heating rates setting at 5, 10, 15, and 20 K min^{-1}. The temperature programmed desorption (TDP) performance of the hydrogenation saturated alloys was test by thermogravimetry measurement under dynamic heating condition (5 K min^{-1}) and 35.1 mL min^{-1} high-purity argon (99.999%) flow rate.

Results and discussion

Structure characteristics

Fig. 1 shows the XRD curves of the as-cast and milled $YMg_{11}Ni$ and $YMg_{11}Ni$ + 5 wt% MoS_2 alloys before and after hydrogenation and dehydrogenation. The hydrogenation reaction occurred at 593 K and 3 MPa, whereas dehydrogenation reaction occurred at 593 K and 1×10^{-4} MPa. The XRD pattern of alloys were identified by ICDD, and the results revealed that two phases appear inside the as-cast alloy, including $Mg_{24}Y_5$ and Mg_2Ni as the major and secondary phases, respectively. Mechanical milling causes diffraction peaks to merge and dramatically broaden, as well as show a typical nanocrystalline and amorphous structure. After adding MoS_2, the diffraction peaks become more broaden, which means the more serious refinement of grains, as Fig. 1(b) shows. After hydrogenation, the alloy exhibits an obvious crystalline reaction, and three hydrides can be found in the $YMg_{11}Ni$ alloy. The hydrides are MgH_2, Mg_2NiH_4, and YH_3. Based on XRD analysis, possible formation pathways of the hydrides can be inferred as follows:[46]

$$Mg_{24}Y_5 + H_2 \rightarrow MgH_2 + YH_2$$

$$YH_2 + H_2 \rightarrow YH_3$$

$$Mg_2Ni + H_2 \rightarrow Mg_2NiH_4$$

Three phases appear in the dehydrogenated $YMg_{11}Ni$ alloy, including YH_2, Mg, and Mg_2Ni. The path of the dehydrogenation reaction can be inferred as follows:

$$MgH_2 \rightarrow Mg + H_2$$

$$Mg_2NiH_4 \rightarrow Mg_2Ni + H_2$$

$$YH_3 \rightarrow YH_2 + H_2$$

YH_2 phase remains undecomposed, which is due to its high thermal stability. Fig. 1(b) shows that adding MoS_2 catalyst does not create any new phase in the pattern, suggesting no reaction between the MoS_2 and any element in the alloy. From the above-mentioned results, the reversible reactions during the hydrogenation and dehydrogenation processes include the following reactions:

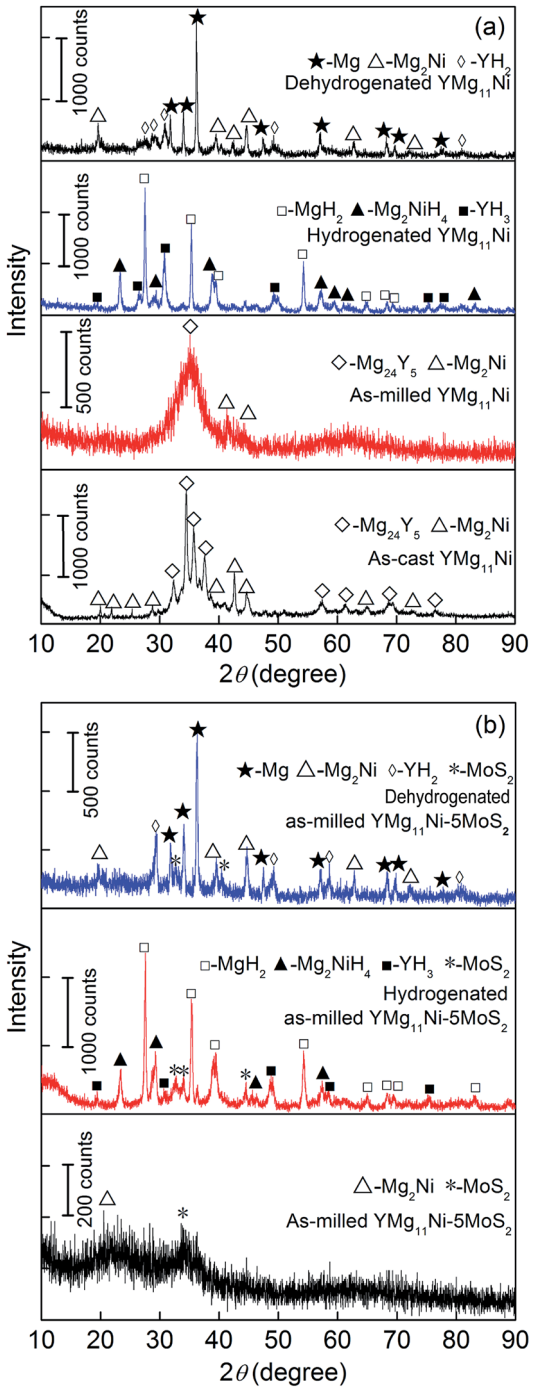

Fig. 1 XRD profiles of the as-cast and milled alloys before and after hydrogen absorption and desorption: (a) $YMg_{11}Ni$, (b) $YMg_{11}Ni$–$5MoS_2$.

$$Mg + H_2 \leftrightarrow MgH_2$$

$$Mg_2Ni + H_2 \leftrightarrow Mg_2NiH_4$$

$$YH_2 + H_2 \leftrightarrow YH_3$$

The HRTEM images and ED patterns of the as-milled $YMg_{11}Ni$ and $YMg_{11}Ni$–$5MoS_2$ alloys before and after

hydrogenation and dehydrogenation are shown in Fig. 2. The as-milled $YMg_{11}Ni$ alloy has a nanocrystalline and amorphous structure with particle size of approximately 15 nm in average. The mechanical milling does not change the alloy of its phase composition, containing the $Mg_{24}Y$ and Mg_2Ni phases, which are also affirmed by the ED patterns analysis. After hydrogenation, the as-milled $YMg_{11}Ni$ alloy still shows a nanocrystalline and amorphous structure (Fig. 2(b)), but the amorphous phase obviously decreases, suggesting that hydrogen absorption facilitates the crystalline reaction. Three hydrides, namely, MgH_2, Mg_2NiH_4, and YH_3, appear in the hydrogenated alloy, which is supported by ED patterns. Fig. 2(c) shows that the dehydrogenated $YMg_{11}Ni$ alloy shows a completely crystalline structure, and the grain sizes visibly grow. Pukazhselvan *et al.*[22] have noticed a similar phenomenon. The structural analysis and ED rings index revealed that three phases appear in the dehydrogenated $YMg_{11}Ni$ alloy, namely, Mg, Mg_2Ni, and YH_2. Apparently, YH_2 maintains undecomposed in the process of hydrogen desorbed, which is consistent with XRD detection. Fig. 2(d) shows that the as-milled $YMg_{11}Ni–5MoS_2$ alloy has a nanocrystalline structure, but compared with the undoped MoS_2 alloy, the grain size is obviously diminished (Fig. 2(a)), suggesting that adding MoS_2 catalyst can enhance the ball milling efficiency. The soft MoS_2 particles are excellent lubrication, which can inhibit the agglomeration and cold welding of alloy particles during milling.

P–C–T curves and hydrogen storage thermodynamics

Fig. 3 shows the *P–C–T* curves of the as-milled $YMg_{11}Ni$ and $YMg_{11}Ni–5MoS_2$ alloys at 593, 613, 633, and 653 K by which the effect of adding MoS_2 on the hydrogenation/dehydrogenation thermodynamics can be examined. The absorbing and desorbing pressure plateaus of the alloys are fairly flat, and the hysteresis ($H_f = \ln(P_a/P_d)$) is relatively small. The addition of MoS_2 catalyst has an insignificant effect on the plateau features of the *P–C–T* curves. Two pressure plateaus appear in each *P–C–T* curve. The higher pressure plateau corresponds to the Mg_2NiH_4, the lower one is MgH_2 that is according to the reported results,[47] which is demonstrated in Mg–10Ni–*x*Mm

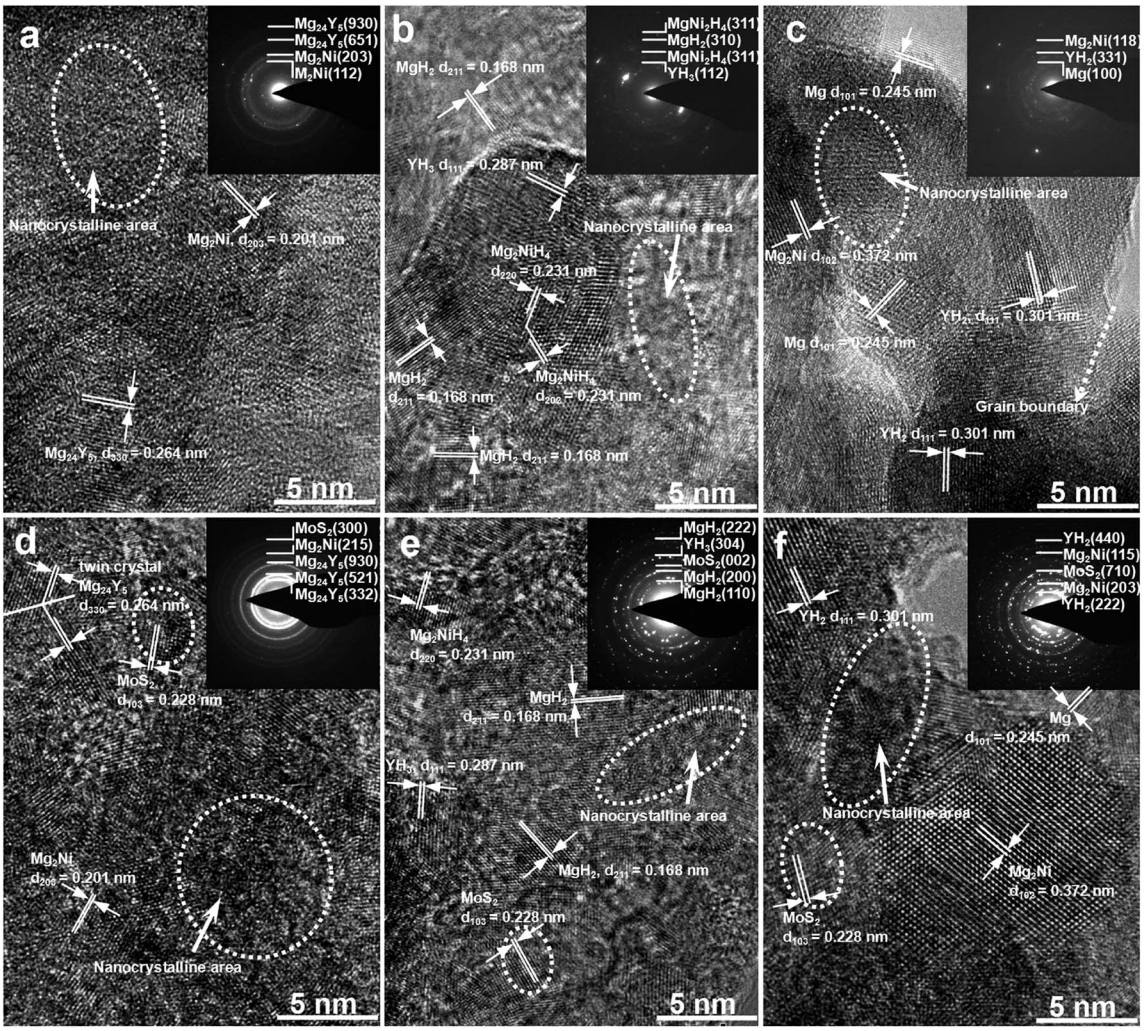

Fig. 2 HRTEM micrographs and SAD patterns of the as-milled alloys at different states: (a) as-milled $YMg_{11}Ni$, (b) hydrogenated $YMg_{11}Ni$, (c) dehydrogenated $YMg_{11}Ni$, (d) as-milled $YMg_{11}Ni–5MoS_2$, (e) hydrogenated $YMg_{11}Ni–5MoS_2$, (f) dehydrogenated $YMg_{11}Ni–5MoS_2$.

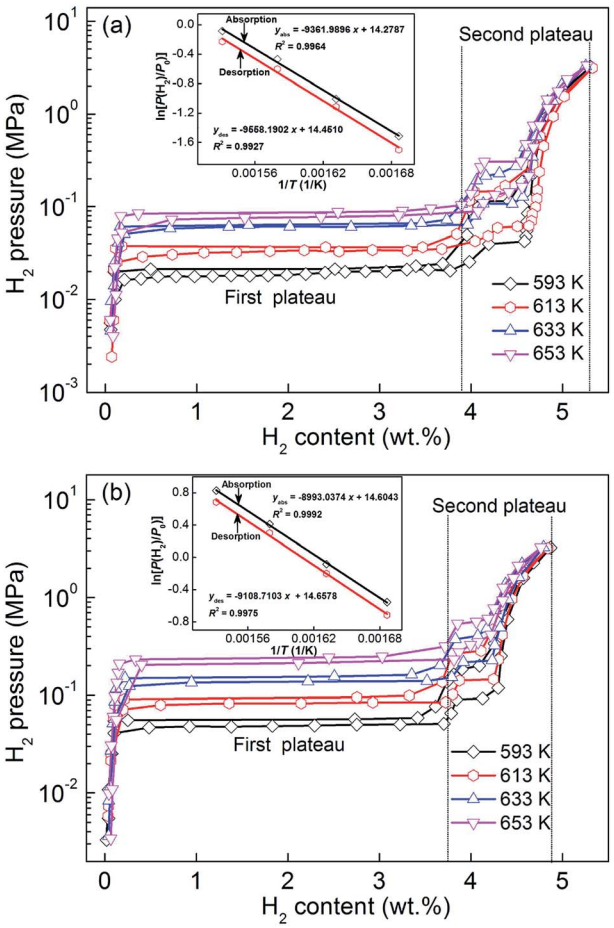

Fig. 3 *P–C–T* curves and Van't Hoff plots of the as-milled (20 h) alloys in the temperature range of 593–653 K: (a) $YMg_{11}Ni$ alloy, (b) $YMg_{11}Ni$–$5MoS_2$ alloy.

alloy.[48] Based on the plateau pressures (P_a and P_d) in Fig. 3, the Van't Hoff equation can be used to calculate the thermodynamic parameters, such as enthalpy change (ΔH) and entropy change (ΔS), as follows:[49]

$$\ln[P(H_2)/P_0] = \Delta H/(RT) - \Delta S/R \quad (1)$$

where $P(H_2)$ represents the equilibrium hydrogen gas pressure (due to having two pressure plateaus, the pressure corresponding to MgH_2 as $P(H_2)$ was selected in this report), P_0 represents the standard atmospheric pressure, T and R represent the sample temperature and gas constant, respectively. The Van't Hoff graphs of $\ln[P(H_2)/P_0]$ *versus* $1/T$ for the $YMg_{11}Ni$ and $YMg_{11}Ni$–$5MoS_2$ alloys can be plotted using the logarithmic transform of eqn (1), as inserted in Fig. 3. With the aid of Van't Hoff plots, the thermodynamic parameters can be calculated conveniently, as listed in Table 1.

These findings indicate that ball milling can reduce the absolute value of hydrogen desorption thermodynamic parameters, and the addition of MoS_2 catalyst into $YMg_{11}Ni$ alloy incurs a further reduction. In addition, the obtained dehydrogenation enthalpies (ΔH_{de}) and entropies (ΔS_{de}) of the second phase are consistent with the reported values of Mg_2NiH_4 in the range of 53.23–72.9 kJ mol^{-1}.[50] The dehydrogenation enthalpies (ΔH_{de}) and entropies (ΔS_{de}) of Mg_2NiH_4 in $YMg_{11}Ni$–$5MoS_2$ are 54.74 kJ mol^{-1} and 113.43 J (K^{-1} mol^{-1}), respectively, which are much lower than those of Mg_2NiH_4 in as-milled $YMg_{11}Ni$ alloy (64.5 kJ mol^{-1}, 122.3 J (K^{-1} mol^{-1})),[50] let alone in as-cast $YMg_{11}Ni$ alloy (63.32 kJ mol^{-1}, 94.89 J (K^{-1} mol^{-1})). As considered by Agarwal *et al.*,[36] the obvious thermodynamic improvement, that is, the destabilization of MgH_2, can be achieved only by reducing the grain size to less than 5 nm, which is difficult to realize by mechanical milling. Cheung *et al.*[16] concluded through theoretical calculation that when the grain size of MgH_2 reduces to approximately 1 nm, its stability will drop drastically. Further study revealed that the thermodynamic change could hardly occur unless its grain size is less than 2 nm. However, Paskevicius *et al.*[51] concluded that MgH_2 has lesser stability when the particle size is approximately 7 nm than the bulk material, whereas Anik *et al.*[5] considered that the addition of transition metals into Mg or alloying with Mg will considerably ameliorate magnesium hydride in its thermodynamics.

Hydrogenation and dehydrogenation dynamics

For investigating the effect of adding MoS_2 on hydrogenation dynamics, the variations of hydrogenation capacity of the as-milled $YMg_{11}Ni$ and $YMg_{11}Ni$–$5MoS_2$ alloys with hydriding reaction time were measured at 3 MPa and different temperatures at 593, 613, 633, and 653 K, as presented in Fig. 4. In the initial stage, the as-milled alloys showed a high hydrogen-absorbing rate. Subsequently, the hydrogen content took a long time to reach saturation. The circumstance that determines the hydrogenation curve characteristics is probably that at which the alloy obtains a hydride layer on its surface in the initial few minutes that may prevent hydrogen from further diffusion and limit the reaction rate. The addition of MoS_2 catalyst engenders a positive contribution to the enhancement

Table 1 Enthalpy change (ΔH) and entropy change (ΔS) of the hydrogenation/dehydrogenation reaction of alloys

Samples	Plateau	ΔH_{ab} (kJ mol^{-1})	ΔS_{ab} (J mol^{-1} K^{-1})	ΔH_{de} (kJ mol^{-1})	ΔS_{de} (J mol^{-1} K^{-1})
As-cast $YMg_{11}Ni$	First plateau (0–4.170 wt% H)	−82.60	−117.78	86.27	118.60
	Second plateau (4.170–5.428 wt% H)	−62.41	−89.67	63.32	94.89
As-milled $YMg_{11}Ni$	First plateau (0–3.907 wt% H)	−77.83	−118.71	79.46	120.15
	Second plateau (3.907–5.311 wt% H)	−54.09	−91.92	58.433	107.87
$YMg_{11}Ni$–$5MoS_2$	First plateau (0–3.749 wt% H)	−74.76	−121.42	75.73	121.86
	Second plateau (3.749–4.881 wt% H)	−50.746	−107.36	54.74	113.43

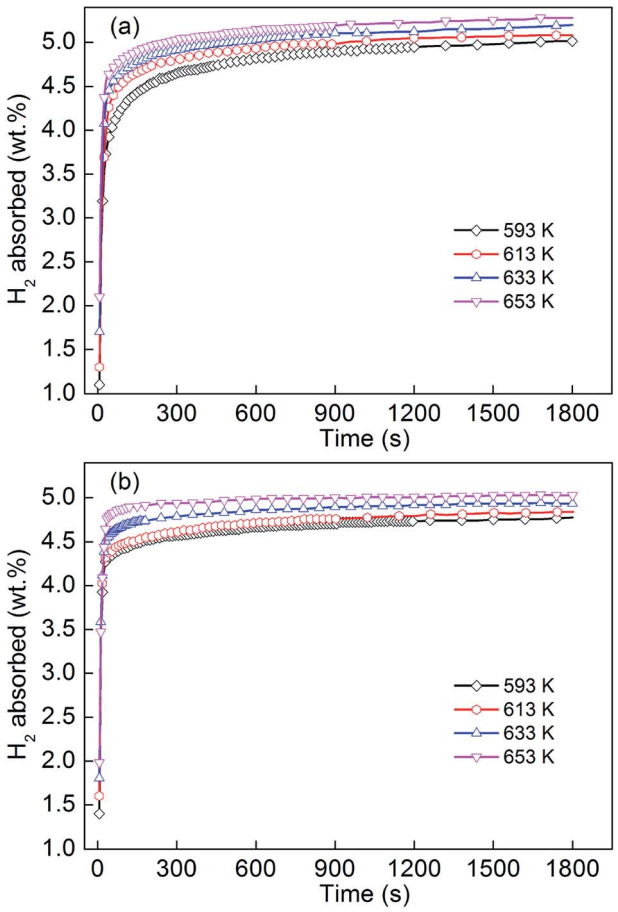

Fig. 4 Hydrogen absorption kinetic curves of the as-milled alloys at different temperatures: (a) $YMg_{11}Ni$, (b) $YMg_{11}Ni–5MoS_2$.

of the hydrogen absorption rate of $YMg_{11}Ni$ alloy. From Fig. 4, the hydrogenation capacities within 60 s at 593, 613, 633, and 653 K are 4.076, 4.399, 4.559, and 4.714 wt%, respectively, for the $YMg_{11}Ni$ alloy and 4.364, 4.422, 4.616, and 4.828 wt%, respectively, for the $YMg_{11}Ni–5MoS_2$ alloy. The addition of MoS_2 compound incurs an obvious catalytic effect on the hydrogenation properties of the alloy. The hydrogenation process of MgH_2 is governed by three critical steps, namely, (a) the dissociation of H_2 from molecule to atom on Mg surface, (b) the diffusion of H atoms along the crystal boundary, and (c) the hydrogenation/dehydrogenation of catalyst and Mg atoms and the transformation of MgH_2 at catalyst/Mg interface. Among all of these steps, step (a) is considered as the rate-controlling factor because of the high energy it requires.[52] Chen *et al.*[53] have reported that atomic Fe can catalyze the dehydrogenation of MgH_2 most because of its polyvalency and moderate strength of electron attraction. Similar to Fe, Mo also has polyvalency. Moreover, Jia *et al.*[54] have demonstrated that Mo is able to facilitate the dissociation of hydrogen. Barkhordarian *et al.*[55] proved that the addition of some catalysts, such as transition metal oxides or sulfide, incurs a decline in this dissociation energy. Therefore, adding MoS_2 particles is speculated to accelerate step (a), that is, facilitate hydrogen dissociation from molecules into atoms. MoS_2 covered on fine alloy grains provides many channels to penetrate hydrogen and active nucleation sites to form MgH_2. Moreover, the added MoS_2 can work as lubricant, which inhibits the agglomeration and cold welding, and improve the effects of ball milling, including the decrease in particle size and increase in surface area-to-volume ratio, consequently facilitating H atoms passing through the hydride and significantly improving the hydrogenation and dehydrogenation dynamics.[56]

At a heating rate of 5 K min^{-1} in a closed chamber, the temperature programmed desorption curve of the as-milled $YMg_{11}Ni$ and $YMg_{11}Ni–5MoS_2$ alloys, which are hydrogenation saturated at 593 K and 3 MPa, were tested as shown in Fig. 5. As the increased pressure can affect the desorption temperature, equal weights of samples were prepared for comparison to avoid this error. Fig. 5 shows that the initial desorption temperature of the as-milled $YMg_{11}Ni$ alloy is approximately 549.8 K, and the total dehydrogenation capacity is 5.286 wt% H_2 by 696 K. The addition of MoS_2 can reduce the initial desorption temperature to approximately 525.8 K. It supports the view of Rafi-ud-din *et al.*[39] that adding catalyst can affect the MgH_2 in initial desorption temperature. The improved desorption behavior, such as the decreased initial dehydrogenation temperature of the alloy, caused by adding MoS_2 might be ascribed to the weakened Mg–H bond that is caused by the electronic exchange reaction between the catalyst and MgH_2, and the similar results have been demonstrated in MgH_2 coated by multi-valence Ti.[57]

To examine the effect of adding MoS_2 on the as-milled $YMg_{11}Ni$ alloy in hydrogen desorption dynamics, isothermal dehydrogenation measurements of the $YMg_{11}Ni$ and $YMg_{11}Ni–5MoS_2$ alloys were conducted at different temperatures, as depicted in Fig. 6. The different temperatures for the isothermal dehydrogenation curves are 593, 613, 633, and 653 K. The temperature variation incurs a significant influence on dehydrogenation dynamics. The increase in temperature dramatically enhances the hydrogen desorption rate of alloys. Fig. 6 shows that the time required by desorbing 3 wt% H_2 at 593, 613,

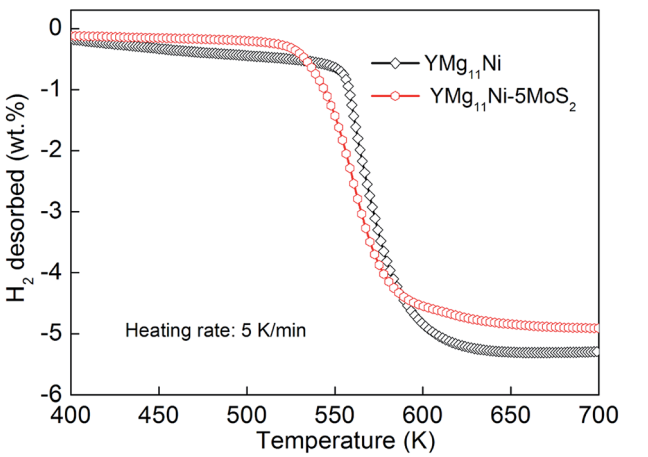

Fig. 5 Temperature programmed desorption curve of the as-milled (20 h) $YMg_{11}Ni$ and $YMg_{11}Ni–5MoS_2$ alloys hydrogenated at a heating rate of 5 K min^{-1}.

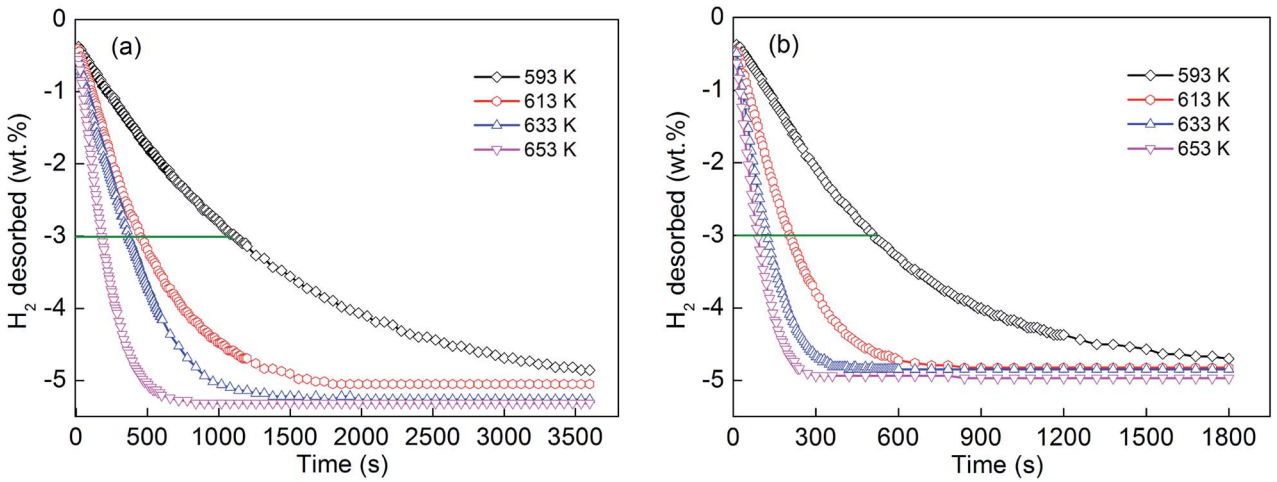

Fig. 6 Hydrogen desorption kinetic curves of the as-milled (20 h) alloys at different temperatures: (a) $YMg_{11}Ni$, (b) $YMg_{11}Ni–5MoS_2$.

633, and 653 K are 1106, 456, 363, and 180 s, respectively, for the $YMg_{11}Ni$ alloy, and 507, 208, 125, and 86 s for the $YMg_{11}Ni–5MoS_2$ alloy. $YMg_{11}Ni$ alloy shows better isothermal desorption dynamics than the no-MoS_2-added $YMg_{11}Ni$ alloy. Thus, MoS_2 is beneficial for the improvement of the dehydrogenation dynamics of $YMg_{11}Ni$ alloy.

Dehydrogenation activation energy

Adding MoS_2 generates a positive contribution to the hydrogen desorption rate of $YMg_{11}Ni$ alloy. To explore the mechanism of this contribution, Arrhenius and Kissinger methods were incurred for estimating the dehydrogenation activation energy of $YMg_{11}Ni$ and $YMg_{11}Ni–5MoS_2$ alloys. The dehydrogenation dynamics is assumed to be connected with the energy barrier for MgH_2 releasing H_2. In general, the total energy barrier that the reaction requires to conquer is signified by activation energy. As for dehydrogenation reaction, the activation energy of which is considered to be related to the whole energy barriers concerning dehydrogenation processes. Therefore, the driving force of a dehydrogenation reaction can be determined by calculating activation energy. The hydrogen desorption reaction is performed through a nucleation and growth processes, which can be simulated by Johnson–Mehle–Avramie (JMA) model and described by the following formula:[58]

$$\ln[-\ln(1-\alpha)] = \eta \ln k + \eta \ln t \quad (2)$$

where α stands for the phase fraction transformed at time t, η stands for the Avrami exponent, and k stands for an effective dynamic parameter. The JMA graphs of $\ln[-\ln(1-\alpha)]$ *versus* $\ln t$ at 593, 613, 633, and 653 K can be constructed using the logarithmic transformation of eqn (2), as illustrated in Fig. 7. The JMA plots are nearly linear, implying that the dehydriding reaction of alloys includes instantaneous nucleation and interface-controlled three-dimensional growth process.[59] Thus, the η and $\eta \ln k$ values at different temperatures can be derived from the slope and intercept of the JMA plots, from which the rate constant (k) could be calculated expediently. According to the Arrhenius equation, the activation energy E_a(de) for the dehydrogenation process can be computed as follows:[60]

$$k = A \exp[-E_a(\mathrm{de})/RT] \quad (3)$$

where k stands for rate constant that has been defined previously, A stands for a temperature-independent coefficient, R stands for the universal gas constant, and T stands for the absolute temperature. The Arrhenius plots of $\ln k$ *versus* $1/T$ for the dehydrogenation dynamics of the alloys are described in Fig. 7. Therefore, the activation energy E_a(de) can be derived from the slopes of the Arrhenius plots. The E_a(de) values of the as-milled $YMg_{11}Ni$ and $YMg_{11}Ni–5MoS_2$ alloys are 98.01 and 85.32 kJ mol^{-1}, respectively. The reduction of 12.7 kJ mol^{-1} occurs in the activation energy, and the similar result has been obtained in $CeH_{2.73}–MgH_2–Ni$ composites, which displays about 41.4 kJ mol^{-1} reduction.[61] This is thought to be the result of the high-density interfacial energy between Mg phase and MoS_2 phase in the $YMg_{11}Ni$ alloy embedded by MoS_2 nanoparticles, which is beneficial for cutting down the distance for H atoms diffusing through the alloys and improving the kinetics. In some other RE–Mg–Ni system alloys, the decrease of activation energy caused by high-density interface required for effective catalysis has been found as well.[57,62–64]

Simultaneously, the hydrogen desorption activation energy is also calculated in Kissinger method for comparison with the following equation:[65]

$$\mathrm{d}[\ln(\beta/T_P/T_P)]/\mathrm{d}(1/T_P) = -E_k(\mathrm{de})/R \quad (4)$$

where β stands for the heating rate, T_p stands for the absolute temperature at which the DSC curve reaches the top desorption rate, E_k(de) stands for activation energy, and R stands for the ideal gas constant. The DSC measurement is indispensable in the Kissinger method, thus the non-isothermal dehydrogenation reactions of as-milled $YMg_{11}Ni$ and $YMg_{11}Ni–5MoS_2$ alloys that hydrogenated at 593 K and 3 MPa were measured by DSC

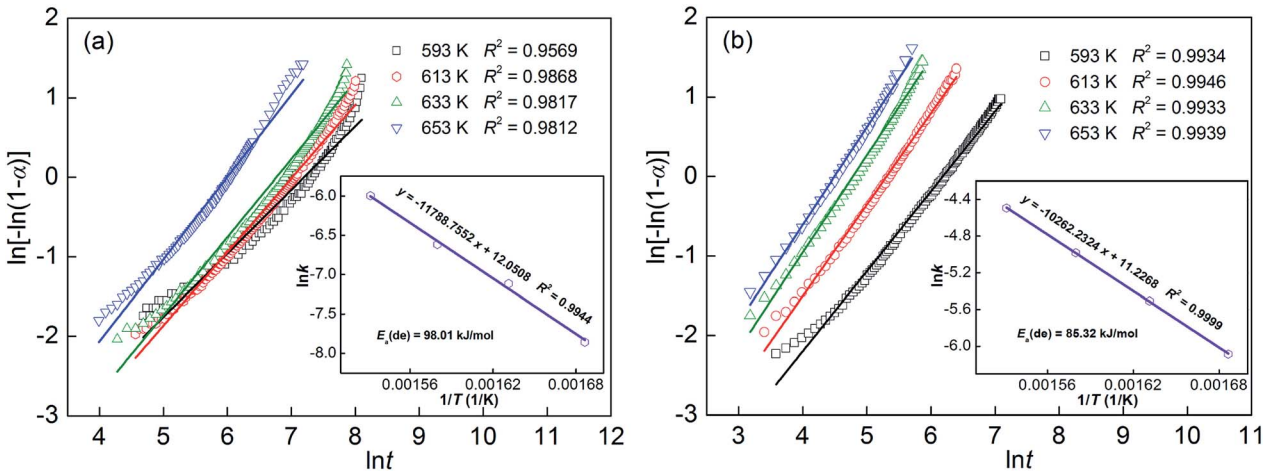

Fig. 7 JMA graphs and Arrhenius plots of the as-milled (20 h) alloys: (a) $YMg_{11}Ni$, (b) $YMg_{11}Ni–5MoS_2$.

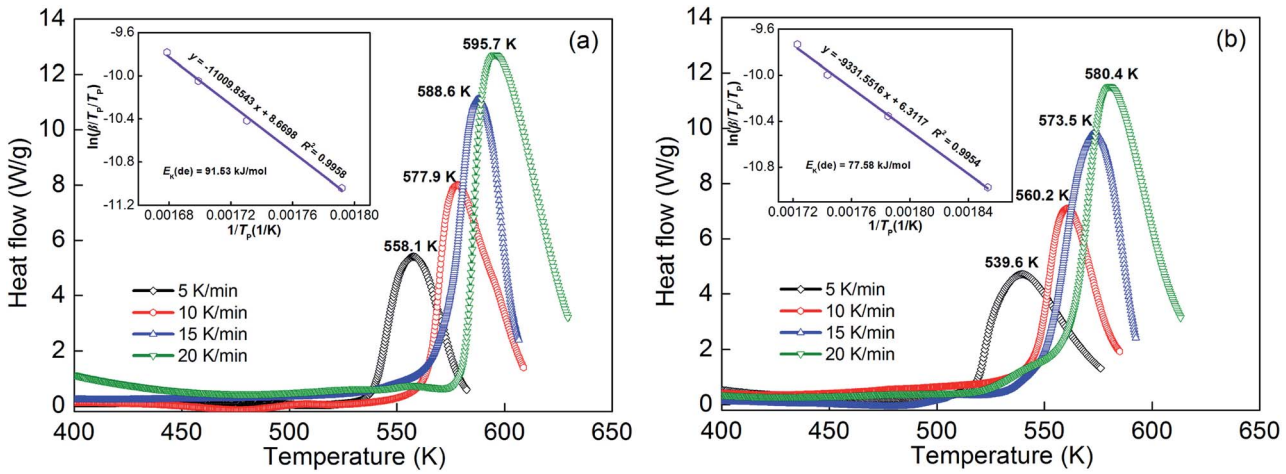

Fig. 8 DSC curves and Kissinger plots of the as-milled (20 h) alloys at various heating rates: (a) $YMg_{11}Ni$, (b) $YMg_{11}Ni–5MoS_2$.

with heating rates at 5, 10, 15, and 20 K min^{-1}, respectively. Results are presented in Fig. 8. During the hydrogenation process, there exists a clear endothermic peak, which is attributed to the dehydrogenation of MgH_2 phase.[66] The endothermic peaks of Mg_2NiH_4/Mg_2Ni and YH_3/YH_2 phase transition can not be verified, which is most likely due to low content of Mg_2NiH_4 and YH_3 in the sample, as well as their endothermic peaks cover the same temperature range. Moreover, the shapes of all endothermic peaks are similar, which indicates that the reaction processes of hydrogenation for all alloys are similar. In addition, the endothermic peak of MoS_2-added alloy drifts to low temperature compared with the no-MoS_2-added alloy at each heating rate, which reflects the improvement of adding MoS_2 in the reaction rate of dehydrogenation. Based on the data of Fig. 8, the graphs of $\ln(\beta/T_P/T_P)$ *versus* $1/T_P$ can be constructed using the logarithmic transformation of eqn (4), which is termed as Kissinger plots as inserted in Fig. 8. The Kissinger plots are nearly linear, from the slopes of which the activation energy E_k(de) can be easily calculated. The E_k(de) values of as-cast $YMg_{11}Ni$ and as-milled $YMg_{11}Ni$ and $YMg_{11}Ni–5MoS_2$ alloys are 125.70, 91.53 and 77.58 kJ mol^{-1}, respectively. Considering the above-mentioned results, ball milling can decrease the dehydrogenation activation energy and the addition of MoS_2 can result in a further decrease, which is assumed to be the real driving force of the improvement of dehydrogenation dynamics. Sun *et al.*[67] considered that the activation energy (E_a) of dehydrogenation is an important indicator in which the dehydrogenation performances and catalytic effects of catalysts can be evaluated. From the reduction of activation energy E_a, we can deduce the reduction of energy barriers for systems releasing hydrogen.

Conclusions

(1) The addition of MoS_2 can reduce the as-milled $YMg_{11}Ni$ alloy in thermodynamic parameters (ΔH and ΔS). Furthermore, it weakens the stability of the alloy hydride. As can be observed from the experiment, the initial dehydrogenation temperature of the $YMg_{11}Ni$ hydrogenated is declined from 549.8 K to 525.8 K by adding MoS_2.

(2) The addition of MoS_2 significantly enhances the alloy in the hydrogen absorbing and desorbing rates, which are connected with the diminished particle sizes and the declined dehydrogenation activation energy generated by adding MoS_2.

(3) The dehydrogenation activation energies of the as-milled $YMg_{11}Ni$ and $YMg_{11}Ni$–$5MoS_2$ alloys have been evaluated in both Arrhenius and Kissinger methods. Results revealed that the addition of MoS_2 can decrease the alloys in dehydrogenation activation energy, which is considered as the real driver for improving the dehydrogenation dynamics of the alloys by adding MoS_2.

Acknowledgements

This work is financially supported by the National Natural Science Foundations of China (51371094 and 51471054) and Natural Science Foundation of Inner Mongolia, China (2015MS0558).

References

1 D. Mori and K. Hirose, *Int. J. Hydrogen Energy*, 2009, **34**, 4569–4574.
2 R. Lan, J. T. S. Irvine and S. Tao, *Int. J. Hydrogen Energy*, 2012, **37**, 1482–1494.
3 L. Zhou, *Renewable Sustainable Energy Rev.*, 2005, **9**, 395–408.
4 V. Bhat, A. Rougier, L. Aymard, G. A. Nazri and J. M. Tarascon, *Int. J. Hydrogen Energy*, 2007, **32**, 4900–4906.
5 M. Anik, F. Karanfil and N. Küçükdeveci, *Int. J. Hydrogen Energy*, 2012, **37**, 299–308.
6 T. Umegaki, J. M. Yan, X. B. Zhang, H. Shioyama, N. Kuriyama and Q. Xu, *Int. J. Hydrogen Energy*, 2009, **34**, 2303–2311.
7 L. Z. Ouyang, J. J. Tang, Y. J. Zhao, H. Wang, X. D. Yao, J. W. Liu, J. Zou and M. Zhu, *Sci. Rep.*, 2015, **5**, 10776.
8 L. Z. Ouyang, Z. J. Cao, H. Wang, R. Z. Hu and M. Zhu, *J. Alloys Compd.*, 2017, **691**, 422–435.
9 L. Z. Ouyang, Z. J. Cao, H. Wang, J. W. Liu, D. L. Sun, Q. A. Zhang and M. Zhu, *J. Alloys Compd.*, 2014, **586**, 113–117.
10 L. Z. Ouyang, Z. J. Cao, H. Wang, J. W. Liu, D. L. Sun, Q. A. Zhang and M. Zhu, *Int. J. Hydrogen Energy*, 2013, **38**, 8881–8887.
11 A. Teresiak, A. Gebert, M. Savyak, M. Uhlemann, C. Mickel and N. Mattern, *J. Alloys Compd.*, 2005, **398**, 156–164.
12 M. Zhu, H. Wang, L. Z. Ouyang and M. Q. Zeng, *Int. J. Hydrogen Energy*, 2006, **31**, 251–257.
13 T. Sadhasivam, M. S. L. Hudso, S. K. Pandey, A. Bhatnagar, M. K. Singh, K. Gurunathan and O. N. Srivastava, *Int. J. Hydrogen Energy*, 2013, **38**, 7353–7362.
14 S. Kalinichenka, L. Röntzsch, T. Riedl, T. Gemming, T. Weißgärber and B. Kieback, *Int. J. Hydrogen Energy*, 2011, **36**, 1592–1600.
15 L. H. Kumar, B. Viswanathan and S. S. Murthy, *J. Alloys Compd.*, 2008, **461**, 72–76.
16 S. Cheung, W. Q. Deng, A. C. T. Duin and W. A. Goddard, *J. Phys. Chem. A*, 2005, **109**, 851–859.
17 J. Huot, G. Liang, S. Boily, A. V. Neste and R. Schulz, *J. Alloys Compd.*, 1999, **293–295**, 495–500.
18 J. X. Zou, X. Q. Zeng, Y. J. Ying, X. Chen, H. Guo, S. Zhou and W. J. Ding, *Int. J. Hydrogen Energy*, 2013, **38**, 2337–2346.
19 M. Jorge Jr, E. Prokofiev, G. F. Lima, E. Rauch, M. Veron, W. J. Botta, M. Kawasaki and T. G. Langdon, *Int. J. Hydrogen Energy*, 2013, **38**, 8306–8312.
20 M. Calizzi, D. Chericoni, L. H. Jepsen, T. R. Jensen and L. Pasquini, *Int. J. Hydrogen Energy*, 2016, **41**, 14447–14454.
21 H. Gu, Y. Zhu and L. Li, *Int. J. Hydrogen Energy*, 2008, **33**, 2970–2974.
22 D. Pukazhselvan, G. Capurso, A. Maddalena, S. L. Russo and D. P. Fagg, *Int. J. Hydrogen Energy*, 2014, **39**, 20045–20053.
23 Y. H. Zhang, X. Y. Han, B. W. Li, H. P. Ren, X. P. Dong and X. L. Wang, *Mater. Charact.*, 2008, **59**, 390–396.
24 S. Kalinichenka, L. Röntzsch, T. Riedl, T. Weißgärber and B. Kieback, *Int. J. Hydrogen Energy*, 2011, **36**, 10808–10815.
25 Y. H. Zhang, Rafi-ud-din, B. W. Li, H. P. Ren, S. H. Guo and X. L. Wang, *Mater. Charact.*, 2010, **61**, 305–311.
26 A. A. Poletaev, R. V. Denys, J. P. Maehlen, J. K. Solberg, B. P. Tarasov and V. A. Yartys, *Int. J. Hydrogen Energy*, 2012, **37**, 3548–3557.
27 K. J. Jeon, H. R. Moon, A. M. Ruminski, B. Jiang, C. Kisielowski and R. Bardhan, *Nat. Mater.*, 2011, **10**, 286–290.
28 M. Tanniru and F. Ebrahimi, *Int. J. Hydrogen Energy*, 2009, **34**, 7714–7723.
29 S. Long, J. X. Zou, X. Chen, X. Q. Zeng and W. J. Ding, *J. Alloys Compd.*, 2014, **615**, S684–S688.
30 Rafi-ud-din, X. H. Qu, P. Li, Z. Lin, A. Mashkoor, I. M. Zubair, M. Yasir Rafique and F. M. Hassan, *RSC Adv.*, 2012, **2**, 4891–4903.
31 N. Juahir, N. S. Mustafa, A. M. Sinin and M. Ismail, *RSC Adv.*, 2015, **5**, 60983–60989.
32 H. Z. Liu, C. Wu, H. Zhou, T. Chen, Y. G. Liu, X. H. Wang, Z. H. Dong, H. W. Ge, S. Q. Li and M. Yan, *RSC Adv.*, 2015, **5**, 22091–22096.
33 X. J. Hou, R. Hu, T. B. Zhang, H. C. Kou, W. J. Song and J. S. Li, *Int. J. Hydrogen Energy*, 2014, **39**, 19672–19681.
34 E. Malka, T. Czujko and J. Bystrzycki, *Int. J. Hydrogen Energy*, 2010, **35**, 1706–1712.
35 F. P. Luo, H. Wang, L. Z. Ouyang, M. Q. Zeng, J. W. Liu and M. Zhu, *Int. J. Hydrogen Energy*, 2013, **38**, 10912–10918.
36 S. Agarwal, A. Jain, P. Jain, M. Jangir, D. Vyas and I. P. Jain, *J. Alloys Compd.*, 2015, **645**, S518–S523.
37 M. Pozzo and D. Alfe, *Int. J. Hydrogen Energy*, 2009, **34**, 1922–1930.
38 T. Liu, T. W. Zhang, X. Z. Zhang and X. G. Li, *Int. J. Hydrogen Energy*, 2011, **36**, 3515–3520.
39 Rafi-ud-din, H. Qu, G. H. Zahid, Z. Asghar, M. Shahzad, M. Iqbal and E. Ahmad, *J. Alloys Compd.*, 2014, **604**, 317–324.
40 M. Daryani, A. Simchi, M. Sadati, H. M. Hosseini, H. Targholizadeh and M. Khakbiz, *Int. J. Hydrogen Energy*, 2014, **39**, 21007–21014.
41 Y. H. Zhang, Z. M. Yuan, W. G. Bu, F. Hu, Y. Cai and D. L. Zhao, *Acta Metall. Sin.*, 2016, **29**, 577–586.

42 Y. H. Zhang, B. W. Li, H. P. Ren, T. Yang, S. H. Guo, Y. Qi and D. L. Zhao, *J. Mater. Sci. Technol.*, 2016, **32**, 218–225.
43 Y. H. Zhang, Z. M. Yuan, T. Yang, D. C. Feng, Y. Cai and D. L. Zhao, *J. Alloys Compd.*, 2016, **688**, 585–593.
44 Y. H. Jia, S. M. Han, W. Zhang, X. Zhao, P. F. Sun, Y. Q. Liu, H. Shi and J. S. Wang, *Int. J. Hydrogen Energy*, 2013, **38**, 2352–2356.
45 D. Liang, S. M. Han, J. S. Wang, W. Zhang, X. Zhao and Z. Y. Zhao, *J. Solid State Chem.*, 2014, **211**, 21–24.
46 T. Yang, Z. M. Yuan, W. G. Bu, Z. C. Jia, Y. Qi and Y. H. Zhang, *Int. J. Hydrogen Energy*, 2016, **41**, 2689–2699.
47 Q. Luo, Q. F. Gu, J. Y. Zhang, S. L. Chen, K. C. Chou and Q. Li, *Sci. Rep.*, 2015, **5**, 15385.
48 J. G. Yuan, N. Xing and Y. Wu, *Int. J. Hydrogen Energy*, 2017, **42**, 6118–6126.
49 H. Falahati and P. J. B. Dominik, *Int. J. Hydrogen Energy*, 2013, **38**, 8838–8851.
50 L. Z. Ouyang, Z. J. Cao, H. Wang, J. W. Liu, D. L. Sun, Q. A. Zhang and M. Zhu, *Int. J. Hydrogen Energy*, 2013, **38**, 8881–8887.
51 M. Paskevicius, D. A. Sheppard and C. E. Buckley, *J. Am. Chem. Soc.*, 2010, **13**, 25077–25083.
52 P. Jain, *Int. J. Hydrogen Energy*, 2009, **34**, 7368–7378.
53 H. P. Chen, H. Yu, Q. Q. Zhang, B. G. Liu, P. Liu, X. P. Zhou, Z. Y. Han and S. X. Zhou, *J. Power Sources*, 2016, **322**, 179–186.
54 Y. H. Jia, S. M. Han, W. Zhang, X. Zhao, P. F. Sun, Y. Q. Liu, H. Shi and J. S. Wang, *Int. J. Hydrogen Energy*, 2013, **38**, 2352–2356.
55 G. Barkhordarian, T. Klassen and R. Bormann, *J. Alloys Compd.*, 2004, **364**, 242–246.
56 E. A. Lass, *Int. J. Hydrogen Energy*, 2011, **36**, 10787–10796.
57 J. Cui, H. Wang, J. W. Liu, L. Z. Ouyang, Q. G. Zhang, D. L. Sun, X. D. Yao and M. Zhu, *J. Mater. Chem. A*, 2013, **1**, 5603–5611.
58 M. Pourabdoli, S. Raygan, H. Abdizadeh and D. Uner, *Int. J. Hydrogen Energy*, 2013, **38**, 11910–11919.
59 T. Czujko, R. A. Varin, C. Chiu and Z. Wronski, *J. Alloys Compd.*, 2006, **414**, 240–247.
60 T. Kimura, H. Miyaoka, T. Ichikawa and Y. Kojima, *Int. J. Hydrogen Energy*, 2013, **38**, 13728–13733.
61 L. Z. Ouyang, X. S. Yang, M. Zhu, J. W. Liu, H. W. Dong, D. L. Sun, J. Zou and X. D. Yao, *J. Phys. Chem. C*, 2014, **118**, 7808–7820.
62 L. Z. Ouyang, F. X. Qin and M. Zhu, *Scr. Mater.*, 2006, **55**, 1075–1078.
63 L. Z. Ouyang, F. X. Qin and M. Zhu, *Scr. Mater.*, 2009, **61**, 339–342.
64 L. Z. Ouyang, S. Y. Ye, H. W. Dong and M. Zhu, *Appl. Phys. Lett.*, 2007, **90**, 021917.
65 H. E. Kissinger, *Anal. Chem.*, 1957, **29**, 1702–1706.
66 H. J. Lin, C. Zhang, H. Wang, L. Z. Ouyang, Y. F. Zhu, L. Q. Li, W. H. Wang and M. Zhu, *J. Alloys Compd.*, 2016, **685**, 272–277.
67 M. Q. Fan, S. S. Liu, Y. Zhang, J. Zhang, L. X. Sun and F. Xu, *Energy*, 2010, **35**, 3417–3421.